



**HAL**  
open science

## Architecture of Fluvial and Deltaic Deposits Exposed Along the Eastern Edge of the Western Fan of Jezero Crater, Mars

Nicolas Mangold, Gwénaél Caravaca, Sanjeev Gupta, Rebecca M E Williams, Gilles Dromart, Olivier Gasnault, Stéphane Le Mouélic, Gerard Paar, James F. Bell, Olivier Beyssac, et al.

► **To cite this version:**

Nicolas Mangold, Gwénaél Caravaca, Sanjeev Gupta, Rebecca M E Williams, Gilles Dromart, et al.. Architecture of Fluvial and Deltaic Deposits Exposed Along the Eastern Edge of the Western Fan of Jezero Crater, Mars. *Journal of Geophysical Research. Planets*, 2024, The Perseverance Rover's Exploration of the Western Fan Front, Jezero Crater, Mars, 129 (3), pp.e2023JE008204. 10.1029/2023je008204 . hal-04521111v1

**HAL Id: hal-04521111**

**<https://hal.science/hal-04521111v1>**

Submitted on 26 Mar 2024 (v1), last revised 26 Apr 2024 (v2)

**HAL** is a multi-disciplinary open access archive for the deposit and dissemination of scientific research documents, whether they are published or not. The documents may come from teaching and research institutions in France or abroad, or from public or private research centers.

L'archive ouverte pluridisciplinaire **HAL**, est destinée au dépôt et à la diffusion de documents scientifiques de niveau recherche, publiés ou non, émanant des établissements d'enseignement et de recherche français ou étrangers, des laboratoires publics ou privés.



Distributed under a Creative Commons Attribution 4.0 International License

**Special Section:**

The Perseverance Rover's  
Exploration of the Western Fan  
Front, Jezero Crater, Mars

## Architecture of Fluvial and Deltaic Deposits Exposed Along the Eastern Edge of the Western Fan of Jezero Crater, Mars

N. Mangold<sup>1</sup>, G. Caravaca<sup>2</sup>, S. Gupta<sup>3</sup>, R. M. E. Williams<sup>4</sup>, G. Dromart<sup>5</sup>, O. Gasnault<sup>2</sup>, S. Le Mouélic<sup>1</sup>, G. Paar<sup>6</sup>, J. Bell<sup>7</sup>, O. Beyssac<sup>8</sup>, N. Carlot<sup>1</sup>, A. Cousin<sup>2</sup>, E. Dehouck<sup>5</sup>, B. Horgan<sup>9</sup>, L. C. Kah<sup>10</sup>, J. Lasue<sup>2</sup>, S. Maurice<sup>2</sup>, J. I. Núñez<sup>11</sup>, D. Shuster<sup>12</sup>, K. M. Stack<sup>13</sup>, B. P. Weiss<sup>14</sup>, and R. C. Wiens<sup>9</sup>

**Key Points:**

- New observations from the Perseverance rover of the western fan front confirm a deltaic origin
- Deltaic foresets in the lower fan front are organized as antiformal structures interpreted as delta mouth bars
- Sandstones and conglomerates in the upper part of the fan front suggest a highly variable fluvial input

**Supporting Information:**

Supporting Information may be found in the online version of this article.

**Correspondence to:**

N. Mangold,  
nicolas.mangold@univ-nantes.fr

**Citation:**

Mangold, N., Caravaca, G., Gupta, S., Williams, R. M. E., Dromart, G., Gasnault, O., et al. (2024). Architecture of fluvial and deltaic deposits exposed along the eastern edge of the western fan of Jezero crater, Mars. *Journal of Geophysical Research: Planets*, 129, e2023JE008204. <https://doi.org/10.1029/2023JE008204>

Received 14 NOV 2023

Accepted 22 FEB 2024

**Author Contributions:**

**Conceptualization:** N. Mangold, G. Caravaca, S. Gupta, R. M. E. Williams, G. Dromart, L. C. Kah, K. M. Stack  
**Data curation:** N. Mangold, G. Caravaca, R. M. E. Williams, O. Gasnault, S. Le Mouélic, G. Paar, J. Bell, N. Carlot, E. Dehouck, J. I. Núñez, K. M. Stack, R. C. Wiens

**Formal analysis:** N. Mangold, G. Caravaca, S. Gupta, R. M. E. Williams, G. Dromart, O. Gasnault, S. Le Mouélic, G. Paar, J. Bell, O. Beyssac, N. Carlot, A. Cousin, E. Dehouck, B. Horgan,

<sup>1</sup>Laboratoire Planétologie et Géosciences, Centre National de Recherches Scientifiques, Nantes Université, Université Angers, Le Mans Université, UMR6112, Nantes, France, <sup>2</sup>Institut de Recherche en Astrophysique et Planétologie, Université de Toulouse 3 Paul Sabatier, CNRS, OMP, CNES, Toulouse, France, <sup>3</sup>Department of Earth Science and Engineering, Imperial College London, London, UK, <sup>4</sup>Planetary Science Institute, Tucson, AZ, USA, <sup>5</sup>Laboratoire de Géologie de Lyon-Terre Planètes Environnement, Université Claude Bernard Lyon 1, Ecole Normale Supérieure Lyon, Centre National de Recherches Scientifiques, Villeurbanne, France, <sup>6</sup>Joanneum Research, Graz, Austria, <sup>7</sup>School of Earth and Space Exploration, Arizona State University, Tempe, AZ, USA, <sup>8</sup>Institut de Minéralogie, de Physique des Matériaux et de Cosmochimie, UMR7590, Centre National de Recherches Scientifiques, Sorbonne Université, Museum National d'Histoires Naturelles, Paris, France, <sup>9</sup>Earth, Atmospheric, and Planetary Sciences, Purdue University, West Lafayette, IN, USA, <sup>10</sup>University of Tennessee, Knoxville, TN, USA, <sup>11</sup>Johns Hopkins University Applied Physics Laboratory, Laurel, MD, USA, <sup>12</sup>Department Earth and Planetary Science, University of California, Berkeley, CA, USA, <sup>13</sup>Jet Propulsion Laboratory, California Institute of Technology, Pasadena, CA, USA, <sup>14</sup>Department of Earth, Atmospheric, and Planetary Science, Massachusetts Institute of Technology, Cambridge, MA, USA

**Abstract** Early observations from the Perseverance rover suggested a deltaic origin for the western fan of Jezero crater only from images of the Kodiak butte. Here, we use images from the SuperCam Remote Micro-Imager and the Mastcam-Z camera to analyze the western fan front along the rover traverse, and further assess its depositional origin. Outcrops in the middle to lower half of the hillslopes comprise planar and inclined beds of sandstone that are interpreted as foresets of deltaic deposits. Foresets are locally structured in ~20–25 m thick, ~80–100 m long, antiformal structures interpreted as deltaic mouth bars. Above these foresets, interbedded sandstones and boulder conglomerates are interpreted as fluvial topset beds. One well-preserved lens of boulder conglomerate displays rounded clasts within well-sorted sediment deposited in overall fining upward beds. We interpret these deposits as resulting from lateral accretion within fluvial channels. Estimations of peak discharge rates give a range between ~100 and ~500 m<sup>3</sup> s<sup>-1</sup>. By contrast, boulder conglomerates exposed in the uppermost part of hillslopes are poorly sorted and truncate the underlying beds. The presence of these boulder deposits suggests that intense sediment-laden flood episodes occurred after the deltaic foreset and topset beds were deposited, although the origin, timing, and relationship of these boulder deposits to the ancient lake that once filled Jezero crater remains undetermined. Overall, these observations confirm the deltaic nature of the fan front, and suggest a highly variable fluvial input.

**Plain Language Summary** Early observations from the Perseverance rover of the Kodiak butte suggested a deltaic origin for the western fan of Jezero crater. Here, we use images from the SuperCam Remote Micro-Imager and the Mastcam-Z camera to analyze the western fan front along the rover traverse, and further assess its origin. We observe strata in the lower part of the fan front that we interpret as deltaic deposits formed below water in a lake. The strata of the upper part of the fan front contain sediments interpreted as fluvial deposits formed under various fluvial regimes, with some of them being deposited by the rivers that also fed the Jezero paleolake. Overall, these observations confirm the deltaic nature of the fan front, and suggest a highly variable fluvial input.

### 1. Introduction

Jezero crater (18.5°N, 77.5°E) hosts the landing site of the NASA Mars 2020 mission, which includes the Perseverance rover and the Ingenuity helicopter. This landing site was selected based on orbital data, indicating substantial fluvial activity with two inlet rivers linked to sedimentary fans (west and north of the crater floor) as well as detection of alteration minerals such as phyllosilicates and carbonates (Ehlmann et al., 2008; Fassett &

© 2024. The Authors.

This is an open access article under the terms of the [Creative Commons Attribution License](https://creativecommons.org/licenses/by/4.0/), which permits use, distribution and reproduction in any medium, provided the original work is properly cited.

L. C. Kah, J. Lasue, S. Maurice,  
J. I. Núñez, D. Shuster, K. M. Stack,  
B. P. Weiss, R. C. Wiens  
**Funding acquisition:** R. M. E. Williams,  
J. Bell, A. Cousin, B. Horgan, L. C. Kah,  
S. Maurice, B. P. Weiss, R. C. Wiens  
**Investigation:** N. Mangold, G. Caravaca,  
S. Gupta, R. M. E. Williams, G. Dromart,  
O. Gasnault, S. Le Mouélic, G. Paar,  
J. Bell, O. Beyssac, N. Carlot, A. Cousin,  
E. Dehouck, B. Horgan, L. C. Kah,  
J. Lasue, S. Maurice, J. I. Núñez,  
D. Shuster, K. M. Stack, B. P. Weiss,  
R. C. Wiens  
**Methodology:** N. Mangold, G. Caravaca,  
S. Gupta, R. M. E. Williams, G. Dromart,  
O. Gasnault, S. Le Mouélic, G. Paar,  
N. Carlot, L. C. Kah, K. M. Stack  
**Project administration:** J. Bell,  
S. Maurice, K. M. Stack, R. C. Wiens  
**Resources:** N. Mangold, G. Caravaca,  
S. Gupta, R. M. E. Williams, G. Dromart,  
O. Gasnault, S. Le Mouélic, G. Paar,  
J. Bell, O. Beyssac, N. Carlot, A. Cousin,  
E. Dehouck, B. Horgan, S. Maurice,  
J. I. Núñez, D. Shuster, K. M. Stack,  
B. P. Weiss, R. C. Wiens  
**Software:** O. Gasnault, S. Le Mouélic,  
G. Paar  
**Supervision:** N. Mangold  
**Validation:** N. Mangold, G. Caravaca,  
S. Gupta, R. M. E. Williams, G. Dromart,  
O. Gasnault, S. Le Mouélic, G. Paar,  
J. Bell, O. Beyssac, A. Cousin,  
E. Dehouck, B. Horgan, L. C. Kah,  
J. Lasue, S. Maurice, J. I. Núñez,  
D. Shuster, K. M. Stack, B. P. Weiss,  
R. C. Wiens  
**Visualization:** N. Mangold, G. Caravaca,  
S. Gupta, R. M. E. Williams, G. Dromart,  
O. Gasnault, S. Le Mouélic, G. Paar,  
J. Bell, N. Carlot, A. Cousin, L. C. Kah,  
S. Maurice, J. I. Núñez, K. M. Stack,  
R. C. Wiens  
**Writing – original draft:** N. Mangold,  
G. Caravaca, S. Gupta, R. M. E. Williams,  
G. Dromart, O. Gasnault, S. Le Mouélic,  
G. Paar, O. Beyssac, A. Cousin,  
E. Dehouck, B. Horgan, L. C. Kah,  
J. Lasue, S. Maurice, J. I. Núñez,  
D. Shuster, K. M. Stack, B. P. Weiss,  
R. C. Wiens  
**Writing – review & editing:** N. Mangold,  
G. Caravaca, S. Gupta, R. M. E. Williams,  
G. Dromart, O. Gasnault, S. Le Mouélic,  
G. Paar, J. Bell, O. Beyssac, A. Cousin,  
E. Dehouck, B. Horgan, L. C. Kah,  
J. Lasue, S. Maurice, J. I. Núñez,  
D. Shuster, K. M. Stack, B. P. Weiss,  
R. C. Wiens

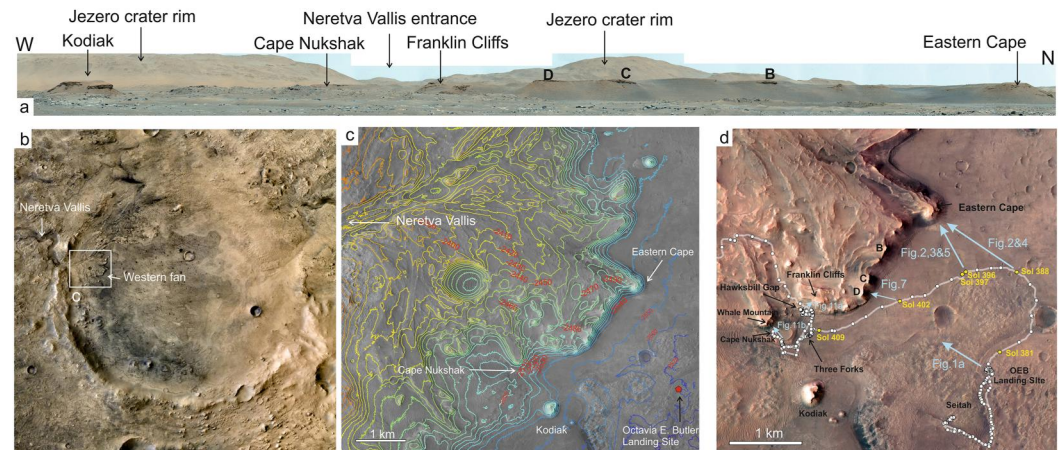


**Figure 1.** (a) Mastcam Z 110 mm mosaic taken on sol 57 of the western fan front viewed from the landing site area. (b) Context image of Jezero crater (Mars Express image, Credit: ESA/DLR/FUBerlin) (c) High Resolution Imaging Science Experiment (HiRISE) orbital data with topographic contours every 10 m of elevation. (d) Color HiRISE image with rover traverse in white and sol numbers in yellow, names of key outcrops treated in this study (in black) and of other locations (in white). Arrows indicate the direction of the images or mosaics displayed in figures.

Head, 2005; Goudge et al., 2012, 2015; Schon et al., 2012). Prior to Perseverance's landing, the existence of a paleolake was suspected within this 45-km diameter crater based on the presence of an outlet river to the east (Fassett & Head, 2005). Based on the observed deltaic architectures of the exposed Kodiak butte, a residual butte of the western fan, early observations from the Perseverance rover confirmed the presence of a paleolake, but the lake level deduced from these images pointed toward a closed system nearly 100 m below the breach to the east of the crater (Mangold et al., 2021).

These initial interpretations were based on remote images obtained by Perseverance from the Octavia E. Butler (OEB) landing site, located more than 2 km from Kodiak and the fan front. In these early observations, the western fan front displayed boulder conglomerates from fluvial floods, but the evidence for a Gilbert delta came exclusively from images of the Kodiak butte (Mangold et al., 2021). Questions remain whether the same deltaic architecture observed at Kodiak was present within the western fan itself. The fluvial deposits also require further investigation to refine the initial interpretations and discharge rate estimations made from the long distance images, and to determine whether these floods were part of the fluvial activity that fed the ancient lake that once filled Jezero crater in the Late Noachian or Early Hesperian, ~3.6–3.7 Ga (Mangold et al., 2020).

Here, we describe observations made along the rover traverse in March and April 2022, between sols 381 to 409 (sols are martian days), from locations north of the OEB landing site, which focused on the eastern and south-eastern eroded edge of the western fan (Figure 1). Most data detailed hereafter were still made at relatively long distances from the rover (400 m–1.5 km), but these new images provide significant improvements to the initial observations and highlight outcrops that were not described previously. The southern fan front (from Franklin Cliffs to Cape Nukshak), where the rover ascended the fan, is treated separately in companion papers (Gupta et al., 2022, Stack et al., this issue). Additional interpretations of the Kodiak butte are given in Caravaca et al. (this issue). The observations and interpretations presented here improve our understanding of the formation and evolution of the western fan, and provide important geologic context for Perseverance's exploration and sampling efforts within Jezero crater.

## 2. Data Sets and Methods

### 2.1. The SuperCam Instrument

SuperCam combines five techniques: imaging through the color Remote Micro-Imager (RMI), Laser Induced Breakdown Spectroscopy to determine elemental chemistry, Raman spectroscopy and reflectance spectroscopy to characterize the mineralogy, and a microphone (Maurice & Wiens, 2021; Maurice et al., 2021; Wiens et al., 2021). Only data from the RMI is used in this paper, which is localized on the Remote Sensing Mast (RSM) and provides high-resolution (2,048 × 2,048 pixel) color images. SuperCam's RMI uses Bayer color filters and is

mounted on a 110 mm diameter Schmidt-Cassegrain telescope with a focal length of 563 mm that can focus to infinite. The angular size of the RMI pixels is 10.1  $\mu$ rad, thus corresponding to approximately 1 cm/pixel at a distance of 1 km. The main correction applied to these images is a division by a reference flat field to compensate for the vignetting of the instrument. RMI images used here (Table S1 in Supporting Information S1) are assembled in mosaics using a fusion algorithm weighted by the angular distance to the center of each image. A final deconvolution step based on a Lucy-Richardson algorithm is used to increase sharpness.

## 2.2. The Mastcam-Z Instrument

The Mastcam-Z instrument is composed of a pair of zoomable stereo multispectral cameras located on the Perseverance rover's RSM. The field of view of the cameras ranged from  $26^\circ \times 19^\circ$ – $6^\circ \times 5^\circ$  degrees from the lowest (26 mm) to highest (110 mm) focal lengths (Bell & Maki, 2021; Bell et al., 2020) (Table S2 in Supporting Information S1). The RSM can move the cameras over  $360^\circ$  in azimuth, enabling co-locations of Mastcam-Z and SuperCam observations. Mastcam-Z can acquire images using red, green, and blue Bayer-patterned filters, and through a set of 11 narrowband filters that spans a wavelength range of 442–1,022 nm (Bell et al., 2020). Mastcam-Z images are calibrated to radiance units using the coefficients derived from the radiometric calibration and converted to radiance factor units (I/F) using images of the Mastcam-Z calibration target (Hayes et al., 2021; Kinch et al., 2020). Mastcam-Z allows for stereo imaging and subsequent 3D vision processing, data fusion with High Resolution Imaging Science Experiment (HiRISE) images satellite Digital Elevation Models (DEMs) and 3D visualization and interpretation (Paar et al., 2023). Geometric calibration (Hayes et al., 2021) ensures the spatial integrity of measurements and interpretations in the Mars-global reference frame across observation-distance depending scales between sub-mm and km.

## 2.3. Orbital Data

Data used in this study include orbital visible images from the Context Camera (CTX, Malin et al., 2007) and HiRISE camera (McEwen, 2007; McEwen et al., 2007) of the Mars reconnaissance Orbiter. Mosaics of these images were assembled in a Geographic Information System. Regional topography was obtained from the Mars Observer Laser Altimeter (MOLA, Smith et al., 1999). For local observations of the Jezero crater entrance, DEMs were constructed using HiRISE stereo image pairs with a spatial resolution of 1 m/pixel (Ferguson et al., 2020).

## 2.4. Local Measurements

Local elevations reported in figures were established by manual referencing of features visible in the rover images in the HiRISE image and DEM, with a confidence of  $\pm 2$  m. Strata strikes reported were obtained from the same comparison between orbital and in situ images. Strata dips reported are apparent dips estimated at  $\pm 5^\circ$  from the rover images. By being apparent dips, they may be locally underestimated. For the clast size distribution analysis in SuperCam/RMI, we selected all clasts visible in the image that were greater than five pixels along their minor axis. This lower bound corresponds to a minimum clast size (5 by five pixels representing  $4.5 \times 4.5$  cm) that can be confidently identified in the image. Clast diameters are measured as the average of long-axis and short-axis.

## 3. Observations and Interpretations

In this section, we focus first on the easternmost observations of the western fan (Figure 1). This escarpment, referred to as scarp “A” in Mangold et al. (2021), is informally named the Eastern Cape. In a second step, we will focus on scarps located southeast of the fan named scarps B, C, and D (Figure 1), as in Mangold et al. (2021).

### 3.1. Eastern Cape

The escarpment at the Eastern Cape is 70 m high and its southeastern face is entirely visible from the rover locations on sols 388, 396, and 397. Scree covers whole sections of the hillslope, but bedrock is exposed at two outcrops imaged by SuperCam RMI: Moro Rock in the lower part of the hillslope, and Miners Castle in the upper part (Figure 2).



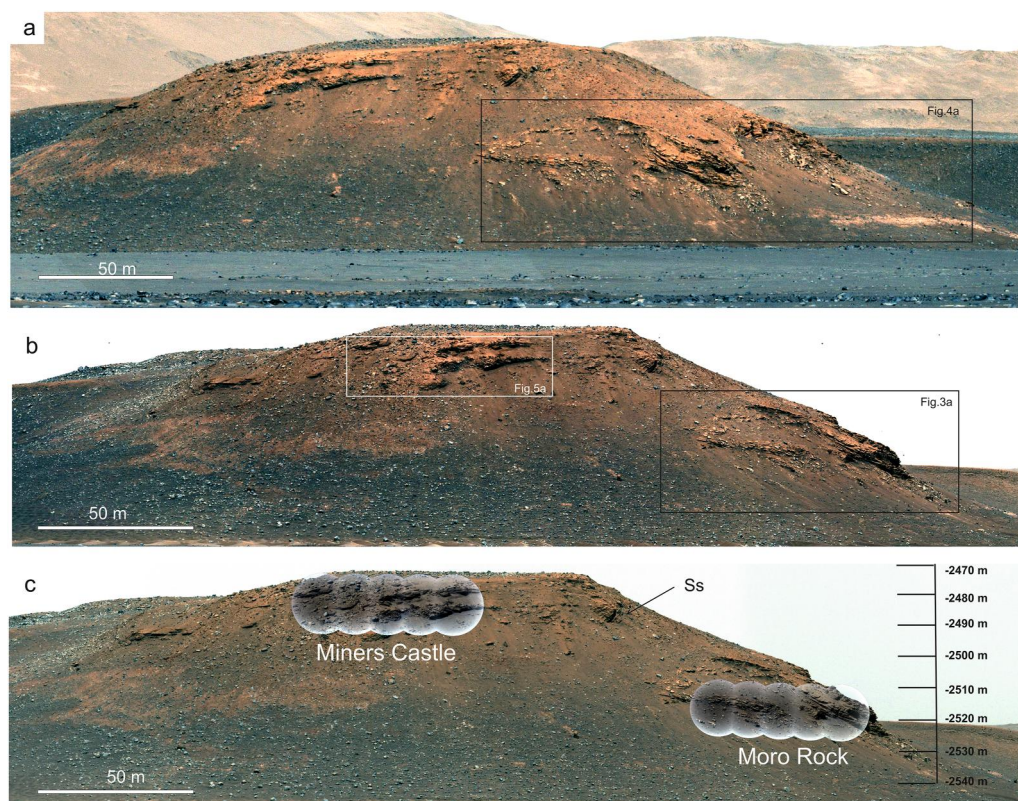


**Figure 2.** Mastcam Z 110 mm mosaic of the Eastern Cape taken on sol 388 (a) and sol 397 (b). (c) Same view as in panel (b) with a scale of elevation from High Resolution Imaging Science Experiment Digital Elevation Model data with a precision estimated of  $\pm 2$  m, the two SuperCam RMIs projected in the MastcamZ image, Moro Rock in the lower section, and Miners Castle in the upper section. Ss indicates the locations of inclined strata of sandstones observed at the same elevation as Miners Castle.

### 3.1.1. Moro Rock Outcrop

The outcrop named Moro Rock occupies the middle section of the Eastern Cape hillslope (Figure 2). Moro Rock is a  $\sim 25$  m high outcrop extending from ca.  $-2,525$  m of elevation at its base (still  $\sim 20$  m above the crater floor) to ca.  $-2,500$  m at its top. The outcrop extends over  $\sim 80$  m laterally. This outcrop was not described in Mangold et al. (2021) because the images available from the landing site were not high enough resolution to determine whether this exposure represented a displaced block or an in-place outcrop. With the new set of images taken from a closer viewpoint (Figures 2 and 3), these rocks appear as a wide and coherent outcrop with a consistent dip showing that it is in place.

The southwestern side of the outcrop (strata S1 in Figure 3) displays strata that dip in the direction of the present day slope toward the southeast although the large amount of scree does not allow us to trace layers through the whole package. Values of dip are nearly as high as the slope, reaching  $\sim 25^\circ$  where beds are best preserved. The northeastern side of the outcrop is better exposed (strata S2 in Figure 3). There, the strata display a sigmoidal geometry with gently dipping layers at the top becoming more steeply inclined and then flattening progressively again toward the base of the outcrop (Figure 3b). These strata are cut abruptly by erosion, indicating that they once extended further east. The apparent dip measured on the RMI images (Figure 3c) reaches a maximum of  $32^\circ$  and decreases toward  $15^\circ$  where strata flatten. The strata dip toward the east, suggesting that the structure of the outcrop has an antiformal (or domal) structure with dips passing from SE (strata S1) to E (strata S2) over a few tens of meters.

The good preservation of the sigmoidal strata permits an analysis of the texture and facies of the outcrop (Figure 3c). RMIs have a pixel scale of  $0.9$  cm/pixel at this distance, enabling observation of cm-sized pebbles. The absence of resolvable pebbles suggests that the outcrop is likely dominated by grains finer than gravel-sized.

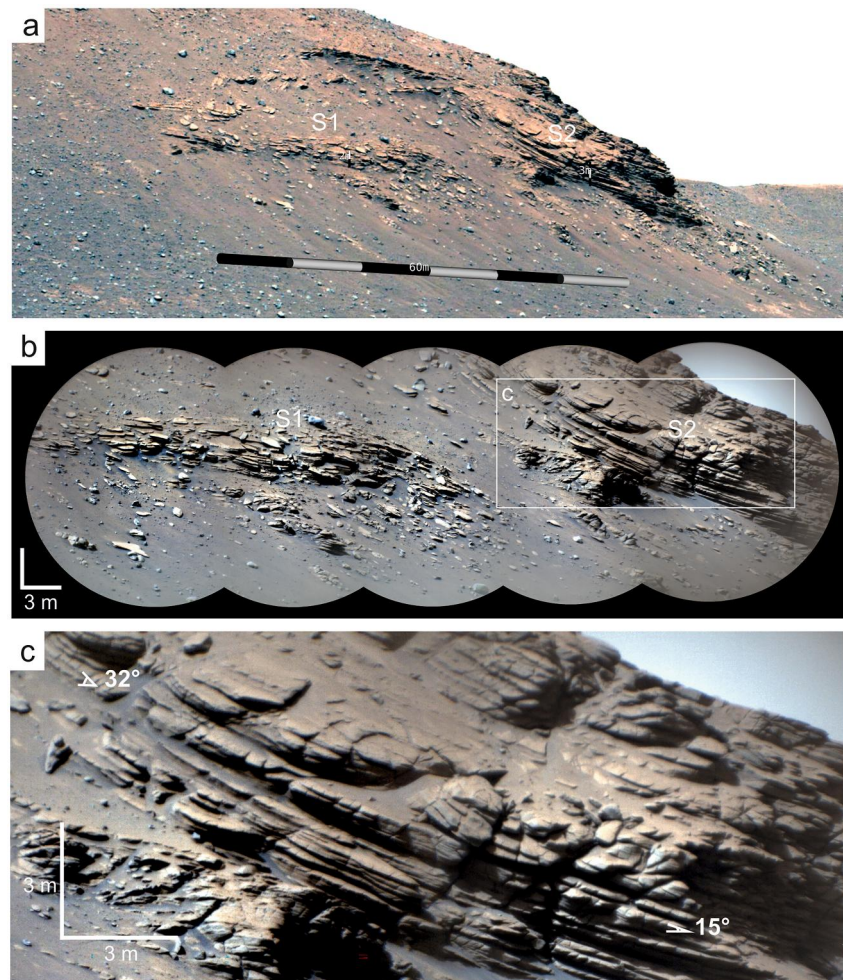


**Figure 3.** (a) Close-up view of Mastcam Z image (sol 397) of Moro Rock with scales obtained from High Resolution Imaging Science Experiment Digital Elevation Model. (b) Mosaic of five SuperCam Remote Micro-Imager images of Moro Rock. (c) Close-up within the SuperCam mosaic on the inclined beds of Moro Rock. The two angles are apparent minimum and maximum dip values. S1 and S2 are the outcropping bed sets described in the text. See Figure 2 for context.

We infer that these rocks are likely sandstones since they are relatively resistant to erosion compared to siltstones and mudstones, which are usually recessively weathering. Strata are composed of planar parallel beds, lacking cross-bedding, onlap, or truncation termination patterns. Sandstone beds have variable thicknesses ranging from 10 to 50 cm, without any apparent periodicity.

A Mastcam Z image provides another view angle enabling the observation of an outcrop located immediately north of Moro Rock at the same elevation (Figure 4a). From their appearance, which is similar to Moro Rock host parallel bedding, and lack cross-stratification, we infer that these strata are composed of planar-bedded sandstones, although no RMIs were acquired here. The orientation of these beds indicates a domal shape of the same range of width (80–100 m) and thickness (20–25 m) as at Moro Rock, although its lateral extension is more difficult to assess. The two domal shapes are annotated as A1 and A2 in Figure 4a. Dip angles and directions have been noted on the orbital image to help their identification in the overall outcrop in the orbital plan view (Figure 4b). These observations point toward a geometry similar to that of Moro Rock.

The Mastcam-Z mosaic shown in Figure 4a also enables a better view of the lower 20 m of the hillside below Moro Rock. Although this lowermost section contains abundant scree, a  $\sim 5$  m thick set of light-toned recessive beds can be observed both in the ground image (light-toned layers (LL) in Figure 4a) and orbital image (LL in Figure 4b). These beds suggest the presence in the lowermost part of the hill slope of fine-grained sediments that are prone to erosion, such as siltstones or mudstones.



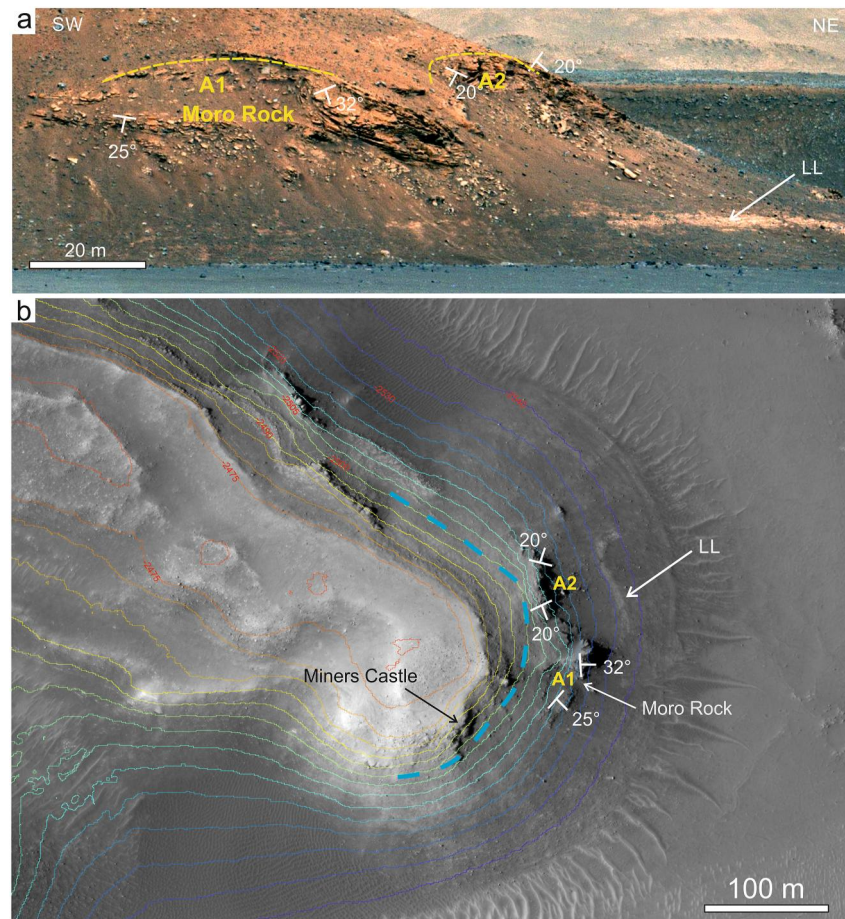


**Figure 4.** (a) Close-up of the Mastcam Z 110 image of sol 388. Light-toned layers (LL) indicates light-toned deposits below the inclined layers. A1 and A2 correspond to the two antiformal shapes with respective apparent dip measurement and orientation. (b) Orbital view with topographic contours (5 m spacing) of Eastern Cape showing the LL, Moro Rock (A1) and the second structure (A2) observed from the ground in panel (a). The dashed blue line represents the potential lake level deduced from the uppermost foreset beds.

### 3.1.2. Miners Castle Outcrop

Above Moro Rock, the widespread presence of scree deposits does not enable continuous observation of strata along the entire hillslope. On the Mastcam Z image (Figure 2c), the upper section of the scarp (elevation ca.  $-2,495$  to  $-2,475$  m) consists of two packages of strata. On the eastern side, right above Moro Rock, there is a series of southward dipping beds (labeled Ss, in Figure 2c) with a maximum thickness of 6 m and a width of  $\sim 30$  m. These strata were interpreted as sandstone (Ss) expressing the lateral accretion of fluvial bars based on the RMI mosaic acquired from the landing area (Mangold et al., 2021). The southern (left) side of the exposure comprises an outcrop composed of boulder conglomerates that was extensively discussed in Mangold et al. (2021). This outcrop has subsequently been named Miners Castle. A new set of RMI images of Miners Castle was taken on sol 397 from 890 m away (Figures 2c and 5). The pixel scale of 0.9 cm/pixel for new observations enables a refinement of previous observations made from the landing area.

The Miners Castle outcrops display two main sedimentary facies: a cobble- and boulder-rich conglomerate close to the base and a boulder-poor set of beds toward the top (Figure 5b). The boulder-rich section of the outcrop presents an asymmetric geometry, reaching 4.5 m high in the thickest portion, and thinning gradually to the north. The new set of images enables the identification of structures within the conglomerate that were not visible from the initial observations made from the landing area. Clear bedding is observed characterized by beds of  $\sim 50$  cm to  $\sim 1$  m in thickness (Figure 5c). In the central area, individual beds contain cobbles (i.e., size of 64–256 mm) at their base that transition sharply into finer grains with only a few or no pebbles in their upper part (as bounded by yellow dashed

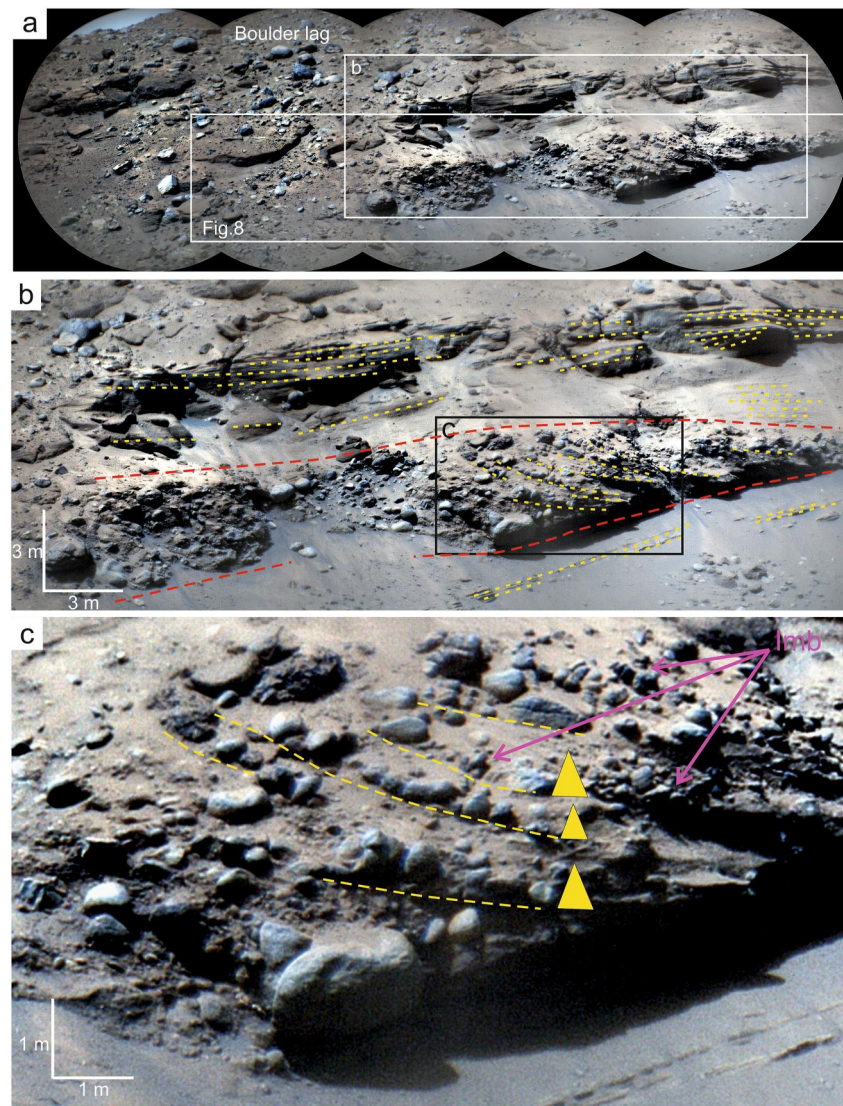


**Figure 5.** (a) SuperCam Remote Micro-Imager mosaic of five images on the Miners Castle outcrops. (b) Close-up of the central part of the outcrops with boulder conglomerates overlain by sandstones (with local cobbles). Yellow dotted line indicates bedding planes. Red dashed lines indicate approximate limits of the conglomerates. Note that the base of the conglomerates seems concordant to the layers of sandstones, without truncations. (c) Detailed view of the cobble and boulder-rich section of conglomerates displaying imbricated cobbles that bound individual beds (yellow dashed lines) with fining upward texture (yellow triangles). Imb indicates imbrication of clasts.

lines in Figure 5c). Such a fining upward sequence (i.e., normal grading) with size-sorted clasts is typical of a decrease in fluid velocity and a change from bedload transport at the base to suspension load in the upper part of a flow (e.g., Leeder, 1982). When pebbles are elongated, they display clast imbrication (labeled Imb in Figure 5c), a geometry also typical of bedload transport in fluvial flows. Many of the clasts here appear significantly rounded or subrounded, suggesting a substantial transport distance, possibly tens of kilometers (e.g., Attal & Lavé, 2006).

With higher resolution images, we have been able to refine the clast size distribution analysis that was previously conducted by Mangold et al. (2021). Our analysis (Table S3) was able to measure four times more clasts than in the initial study (1,442 compared to 333 previously). The new distribution indicates a slightly modified mean diameter (D50) of 7.8 cm and a D84 (diameter below which are 84% of clasts) of 15.2 cm (Figure 6), compared to D50 of 16.4 cm and D84 of 25.2 cm in Mangold et al. (2021). This difference does not substantially modify previous conclusions about the type of conglomerates or the flow regime, but it enables a refinement of the discharge rate calculations for which the grain size distribution is one of the input parameters (Section 4).



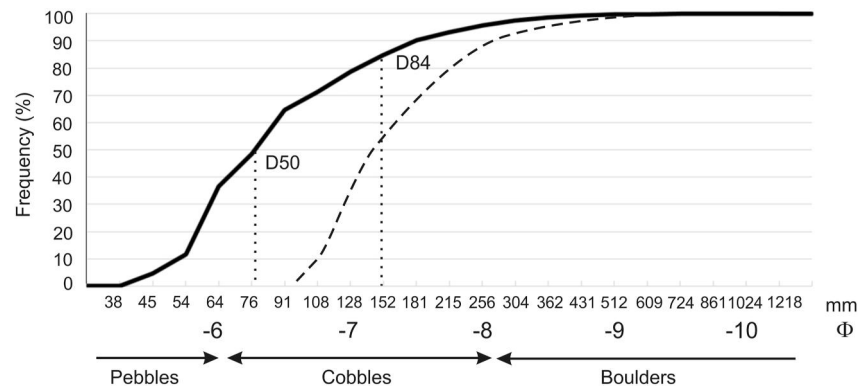


**Figure 6.** Cumulative histogram on a logarithmic scale ( $\phi$  scale defined by  $\log_2$  increments) of the measured sizes of 1,442 clasts (solid curve) compared to the previous measurements made from 333 clasts in Mangold et al. (2021) (dashed curve). Dotted lines indicate the new measurements of D50 and D84.

More strata are observed above the bedded cobble-boulder conglomerates (Figure 5b). This 4–5 m thick section comprises sandstone, pebble-rich sandstone, and pebble- and cobble-conglomerates. Locally, cross-bedding can be observed within these subhorizontal beds.

Atop these outcrops lies a residual lag of subrounded cobbles and boulders (indicated as boulder lag at the top of Figure 5a). The presence of partly buried boulders of up to 2 m in the long axis suggests that the lag was initially more than 2 m thick. The presence of these boulders indicates that more conglomerate beds overlay the previously described beds but have been subsequently eroded into vestigial boulders and cobble lags.

### 3.2. Other Fan Scarps of Interest Toward the Southeast

The hillslopes observed several hundred meters to the SW of the Eastern Cape and oriented toward the southeast are largely covered by scree except their uppermost section, which exposes rock outcrops that are between 6 and 10 m tall (Figures 1 and 7).

Starting from the south, scarp D displays a 6 m thick section whose upper 4 m is dominated by boulders (Figure 7b). This boulder-rich facies lacks apparent bedding or sorting, and shows strongly variable boulder sizes up to 1.5 m in the long axis. This boulder conglomerate (Bcg) is underlain by finer-grained facies (Ss), likely sandstone or finer, that is weathered in place. The thickness of sandstones is at least 2 m, but their full vertical extent cannot be determined because of scree cover. Scree and dust also impede the clear identification of sedimentological features within this sandstone. The contact between conglomerates (Bcg) and sandstones (Ss) appears sharp and irregular, suggesting a truncation of the sandstone by the boulder conglomerate.

The best-preserved section of scarp C displays a similar succession (Figure 7c) with subhorizontal strata at the base overlain by boulder conglomerate (Bcg) composed of many clasts >1 m in size. The boulder conglomerates observed in the upper 2 m lack bedding and are poorly sorted. In contrast to scarp D, the subhorizontal strata here (Ss) are well-preserved, extending over 8 m of the 10 m thick section. They seem composed predominantly of sandstone but pass locally to conglomerate with pebbles and a few cobbles (Cg in Figure 7c). The contact between the subhorizontal strata and the uppermost boulder conglomerate is unconformable, indicating an erosional truncation of the underlying sandstones by the conglomerates.

Discontinuous exposure of strata can be observed northeast of scarp C (Figure 7d). Here, subhorizontal beds continuing from Figure 7c have been largely eroded; only a few of them can be observed locally above the dashed blue line. Below this blue line located ca. –2,490 m, several inclined beds are observed over approximately 20 m of elevation. These strata, which form a distinct package with an apparent dip 10–15° toward the northeast, display parallel bedding and a texture similar to the overlying subhorizontal beds (inferred sandstone).

Scarp B (Figure 1) has not been observed with better images than in Mangold et al. (2021), and is very similar to scarp C, with sandstone truncated by the uppermost boulder conglomerate. Thus, we do not describe this outcrop further hereafter.

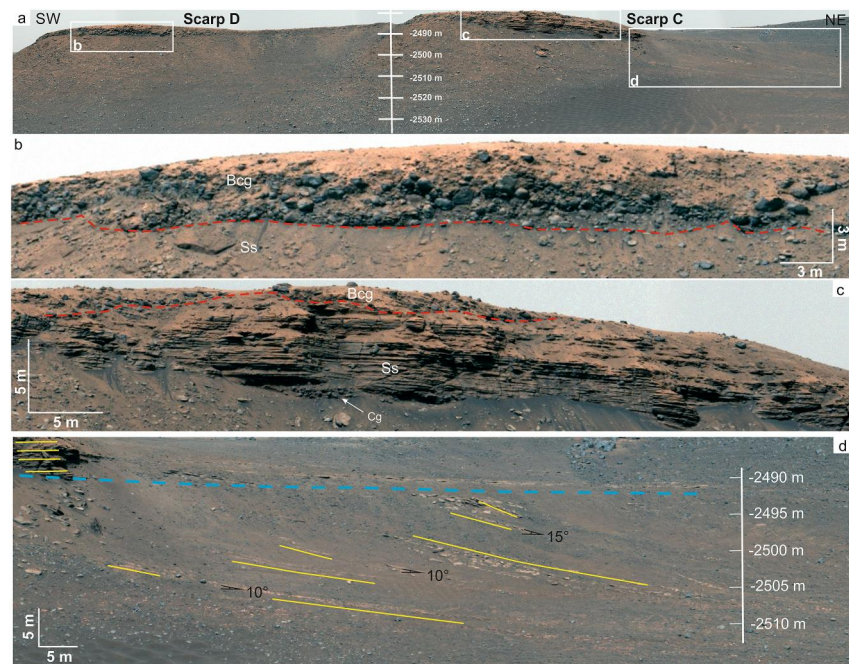


**Figure 7.** (a) Mastcam Z 110 mm image taken on sol 402 of the scarps D (to the left) and C (to the right) localized southwest of Eastern Cape (see Figure 1). Elevation provided based on High Resolution Imaging Science Experiment Digital Elevation Model at a precision of  $\pm 2$  m that may not be valid on the whole length of the panorama due to variations in distances. (b) and (c) are close-ups of the uppermost part of scarps D and C, respectively. On both (b) and (c), Ss, Bcg, and Cg indicate sandstone, boulder conglomerate and conglomerate, respectively. The red, dashed line indicates the sharp transition from subhorizontal sandstone to boulder conglomerate. (d) Is a close-up on the eastern side, mid-slope of scarp C where beds are dipping gently to the NE. The dashed blue line indicates the transition from the subhorizontal strata at the top to the dipping strata.

Due to the abundance of scree, these three scarps give us a partial view of the stratigraphy. The inclined beds in the mid-slope of scarp C have a lower dip than the dipping beds of Moro Rock ( $15^\circ$  at maximum compared to  $32^\circ$ ), but their presence in the same range of elevation ( $-2,510$  m to  $-2,490$  m) and their similar vertical extent suggests that they are part of the same facies of dipping strata. Compared to Miners Castle, which is bedded, and sorted, the outcrops of boulder deposits at scarps C and D are rather chaotic, structureless and poorly sorted. These scarps are comparable to those observed at the top of the Kodiak remnant butte, where sandstones are similarly truncated by poorly sorted boulder conglomerates (Caravaca et al., this issue; Mangold et al., 2021).

#### 4. Discharge Rate Estimations at Miners Castle

The improvement in imaging quality and the related interpretations enable us to refine the discharge rate calculations proposed by Mangold et al. (2021). The Darcy-Weisbach equation can be applied to estimate water discharge rates (hereafter  $Q$ ) for past channels where measurements of width  $W$ , water height  $H$ , slope  $s$  and clast size distribution can be measured (e.g., Bathurst, 1985; Kleinhans, 2005) with a modification related to the use of local Martian gravity  $g_m$  ( $3.72 \text{ m s}^{-2}$ ):

$$Q = A(8g_m R s / f)^{1/2} \quad (1)$$

Here,  $A$  is the cross-sectional area, and  $R$  is the hydraulic radius, which is the ratio between the cross-sectional area  $A$  and the wetted perimeter  $P$ . Parameter  $f$  is an empirical friction factor related to the roughness at the channel bottom. Field and laboratory studies have provided potential values for the friction factor  $f$  as a function of the flow regime and grain size of the channel bed (Kleinhans, 2005). Hereafter, we used two equations taking, for the first one, the mean clast size  $D_{50}$  and a gravel bed (Kleinhans, 2005) and, for the second one, the  $D_{84}$  and a boulder bed (Wilson et al., 2004):



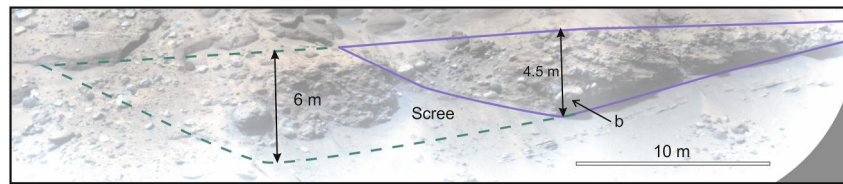


**Figure 8.** Sketch with channel dimensions taken for discharge rate calculations. In purple the 30 m wide channel reached 4.5 m at maximum depth. In dashed green line, a 44 m wide channel reaching 6 m at maximum depth. The shape of channels can be approximated by a triangular shape. See Figure 5a for context.

$$(8/f)^{1/2} = 2.2(R/D_{50})^{-0.055} s^{-0.275} \quad (2)$$

$$(8/f)^{1/2} = 5.62 \log 10(R/D_{84}) + 4 \quad (3)$$

The second equation is relevant given the presence of many boulders.  $D_{50}$  and  $D_{84}$  are taken from the clast size distribution (Figure 6), thus  $D_{50} = 0.078$  m and  $D_{84} = 0.152$ .

For the estimation of the channel geometry, we used the apparent channel shape of the boulder conglomerates (Figure 8). A strict minimum can be determined by using the extent of conglomerate deposits, which is measured as 30 m in width, where the lateral accretion of beds can be used to estimate the minimum channel depth, in this Case 4.5 m (blue contours in Figure 8). However, the conglomerate extends laterally to the left of the outcrops, suggesting the channel may have been larger. Thus, this larger extent (green dotted line in Figure 8) represents an upper bound for the channel dimension, reaching 44 m in width and 6 m in depth. In contrast to most calculations of discharge rates, which use rectangular areas for the channel section, we use a triangular shape that corresponds to the geometry observed, and provides a more realistic measurement of the wetted perimeter.

Channel depths follow an empirical rule for bankfull flows in terrestrial rivers (Konsoer et al., 2018):

$$H = 0.164W^{0.66} \quad (4)$$

This scaling law is assumed not to differ significantly from Earth on Mars despite its lower gravity (Konsoer et al., 2018). Values deduced from this law suggest water channel depths of 1.55 and 1.99 m for 30 and 44 m wide channels, respectively, which are lower than the observed maximum values. However, these estimated values are average depths from empirical data, and not maximum depths. Estimated depths of 4.5 and 6 m are actually local maxima, but an average channel depth, which is equivalent to the hydraulic ratio  $R$ , measured by the ratio between  $W$  and the wetted perimeter  $P$ , is found to be 1.87 and 2.53 m, for both channel dimensions (30 and 44 m), respectively. These values are close to the empirical values estimated from the terrestrial law.

The slope at the base of the conglomerate has been estimated by Mangold et al. (2021) as  $s = 0.014$ , slightly higher than the slope at the top of the plateau ( $s = 0.012$ ). An upper bound was also taken as  $s = 0.029$  (Mangold et al., 2021) from the slope below the boulder conglomerate in the C and D scarps. However, our new observations (Section 3.2) raise the point that boulder conglomerates of scarps C and D might correspond to a distinct flood event rather than the fluvial flow of Miners Castle. Indeed, (Bcg) in scarps C and D are structureless, non-sorted and truncate the underlying sandstones, in contrast to Miners Castle, which is well-bedded, sorted and does not truncate the underlying sandstones. Hence, this higher bound is no longer justified and we use only the value of 0.014.

The values of discharge rates using these parameters vary from 126 to 521  $\text{m}^3 \text{s}^{-1}$  (Table 1). These values still represent a relatively large range of estimations, but with a smaller upper bound compared to Mangold et al. (2021), in which values up to 3,000  $\text{m}^3 \text{s}^{-1}$  were reported. This difference is due to for a large part to the refinement in channel shape thanks to the better resolved images, and for a small part to the new grain size distribution.

To better constrain the discharge rates, we propose using another method that takes into account the presence of boulders. While efforts to derive the velocity of the flow from boulders started with empirical measurements (Costa, 1983), several authors have tried to estimate this velocity from theoretical calculations. One of the most

**Table 1**  
*Discharge Rates Estimated for Miners Castle Fluvial Conglomerates*

Width (m)	Maximum height (m)	D50 (m)	Velocity gravel bed (Equation 2) (ms <sup>-1</sup> )	$Q$ (Equation 2) (m <sup>3</sup> s <sup>-1</sup> )	D84 (m)	Velocity boulder bed (Equation 3) (ms <sup>-1</sup> )	$Q$ (Equation 3) (m <sup>3</sup> s <sup>-1</sup> )	Velocity to transport large boulder (Equation 4) (ms <sup>-1</sup> )	$Q$ (Equation 5) (m <sup>3</sup> s <sup>-1</sup> )
30	4.5	0.076	1.86	<b>126</b>	0.152	3.17	<b>213</b>	2.11	<b>142</b>
44	6	0.076	2.14	<b>282</b>	0.152	3.95	<b>522</b>	2.11	<b>278</b>

*Note.* Channel dimensions are estimated from the triangular shapes in Figure 8. Slope is fixed at 0.014 from Mangold et al. (2021). Discharge rates obtained by three methods are in bold. See Section 4 for explanation.

recent attempts (Alexander & Cooker, 2016) is based on the net force acting upon a boulder during a flood being defined as the sum of the drag-force and an impulsive force resulting from the initial acceleration and subtracting the frictional force. They derive from these assumptions a value for the velocity of

$$V^2 = 4/3Dg\left(\left(\rho_b/\rho_f - 1\right)\mu - ka/g\right) \quad (5)$$

where  $\rho_b$  and  $\rho_f$  are, respectively, the volumetric mass of the boulder (taken at 3,000 kg.m<sup>-3</sup> for a basalt) and that of the fluid (taken at 1,000 kg.m<sup>-3</sup>).  $D$  is the boulder average size and  $k$  depends on the aspect ratio of the boulder, which is the ratio of the long axis over the sum of long and short axes, set up at 0.5 for a sphere. The two parameters  $\mu$  and  $a$  correspond to the friction coefficient and the initial acceleration of the boulder, respectively. Alexander and Cooker (2016) have fixed these two parameters from empirical data on Earth in fluvial rivers transporting boulders, as  $\mu = 0.4$  and  $a = 0.5$ . Lacking any similar work on Mars, we use the same empirical parameters in our calculation.

To apply this calculation of Equation 5, we use a large hanging boulder (b in Figure 8) at the base of the channel to represent the largest clast transported. This subrounded boulder is imbricated within cobbles and was clearly transported by the flow. With its average size  $D$  of 1.25 m, and aspect ratio  $k$  of 0.63, we obtain a flow velocity of 2.11 m s<sup>-1</sup>. Using the two possible channel geometries proposed (Table 1), we obtain discharge rate estimations of 142–278 m<sup>3</sup> s<sup>-1</sup> by this method, which are taken as the minimum discharge rates required to dislodge and transport boulders of such a size. It is noteworthy that these values are close to the lower estimates of flow made using Darcy-Weisbach equations.

It should also be noted that these estimates are peak discharge rates enabling the transport of boulders in the observed layer, but may not be representative of the average water flow rate entering Jezero crater over longer timescales. Indeed, the variability of sediments from sandstone (as those labeled Ss in Figure 2c) to well organized boulder conglomerates (as in Miners Castle) and poorly sorted conglomerates (as in scarps C and D) suggests highly variable flow regimes.

## 5. Facies Synthesis and Stratigraphic Column

From bottom to top, the strata of these various outcrops can be divided into four major groups, ignoring scree (Figure 9). Firstly, a light-toned recessive unit, corresponding likely to mudstones or siltstones, is observed in the lower part of the Eastern Cape (LL in Figure 4). Its location in the section, tone and low resistance to erosion makes it very similar to rocks exposed at Hogwallow Flats (with the Hawksbill Gap area, Figure 1), an interval that is ubiquitous in orbital images of the southern delta front and that has been interpreted as lake beds (Hogwallow Flats member in Stack et al., this issue). From this comparison and our local observations, we interpret that this bed was deposited in a quiet depositional environment such as that expected for lacustrine deposits.

Steeply dipping sandstone is observed between elevations of ca. -2525 and ca. -2,500 m at the Eastern Cape. Their planar geometry, lack of cross-stratification and locally steep dips (up to 32°) point toward gravity-related deposition by avalanching in a subaqueous delta-front slope environment. Given the thickness of the deposits and their geometry (Figures 3 and 4), we infer that these beds are delta front foresets (e.g., Gilbert, 1885; Longhitano, 2008; Nemeč, 1990; Postma, 1990; Rohais et al., 2008) deposited within a lake rather than fluvial bars formed by lateral accretion. Meander belts could display an antiformal shape in point bar deposits (e.g., Ghinassi



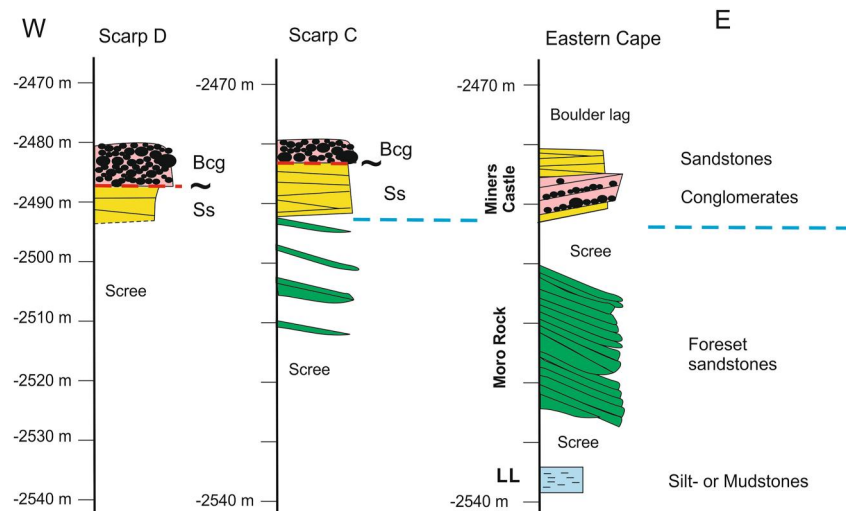


**Figure 9.** Stratigraphic columns of scarps D, C and Eastern Cape (from W to E). The facies corresponding to each color are indicated to the right for all columns. The dashed red lines indicate a truncation or discontinuity below the boulder conglomerates of scarps C and D. The dashed blue lines indicate the transition from lacustrine to fluvial deposits. The names of locations are indicated for the Eastern Cape.

et al., 2014; Willis, 1989), but the scale of the latter would be genetically linked to the width and depth of the meandering channel. These dimensions are not consistent with our observations. Indeed, applying Equation 4, if these were fluvial bars, it would require a  $\sim 1,500$  m wide channel to account for  $a > 20$  m thickness. Such a large channel size is inconsistent with the observation of dome shaped structures (A1 and A2) that have a limited extent of 100 m, that is, the 20 m thick 100 m large structure cannot represent the channel geometry. Meander belts can display antiformal shapes along strike sections through point bar deposits (e.g., Ghinassi et al., 2014; Willis, 1989), but their scale is genetically linked to the width and depth of the meandering channel. The bankfull channel depth  $H$  in a meander belt is linked to the meander-bend radius of curvature  $R_c$  by the empirical relation (Williams, 1986):

$$D = 0.085R_c^{0.66} \quad (6)$$

This relation translates into  $R_c = 3,600$  m for a 20 m deep channel, a value much higher than the  $\sim 100$  m width indicated by the A1 and A2 bodies; a strong difference that is unlikely to be explained by gravity effect.

From their position in the stratigraphy and their vertical extent  $> 20$  m, we interpret the dipping beds of scarp C (Figure 7d) as foreset beds. Their more gentle dip ( $10\text{--}15^\circ$ ) may be related to the gentler delta front slope at this location or to the presence of paleo-relief. The single section orientation does not allow us to determine whether these layers at scarp C were part of a similar lobe structure as A1 and A2 at the Eastern Cape.

The boulder conglomerate observed at Miners Castle as well as the sandstone observed laterally (outcrop Ss in Figure 2c) and that at the top of Miners Castle are all consistent with fluvial deposition from relatively energetic floods, with peak discharge rates estimated in the range of  $\sim 100\text{--}\sim 500$   $\text{m}^3 \text{ s}^{-1}$  for the conglomerate. Their organization as meter-thick dipping beds with normal grading (Figure 5c) suggests lateral accretion typical of sinuous, possibly meandering, rivers. These outcrops lie only a few meters of elevation above the level that records subaqueous deposition of foreset beds. No obvious truncation is observed below the boulder conglomerate, suggesting that it was deposited as fluvial topset beds coeval with the presence of a lake in Jezero crater.

A lateral equivalent of these fluvial deposits may be represented by bedded sandstone and conglomerate observed in scarps C and D. At scarp C, these subhorizontal beds lie immediately above the dipping layers interpreted as foresets, thus as expected for a topset-to-foreset transition on a delta front (materialized by the dashed blue line in Figure 7d). At scarp D, it is possible that these sandstones also represent topset beds, but scree impedes the identification of underlying foreset beds within the lower part of the hillslope. The topset-foreset transitions both at Moro Rock and scarp C are of ca.  $-2,490\text{--}2,500$  m, thus is at a similar elevation range to that observed within Kodiac (Caravaca et al., this issue; Mangold et al., 2021).

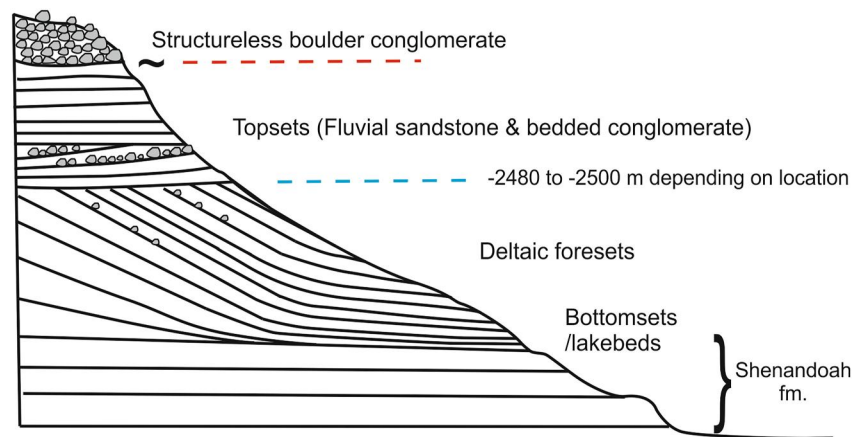


**Figure 10.** Sketch compiling the observations made on several scarps of the fan front in one synthetic section of the western fan of Jezero crater. The Shenandoah formation is defined in Stack et al. (this issue). The dashed blue line indicates the inferred past lake level at the time of deposition, with varying elevation depending on the location. The dashed red line indicates the truncation by the uppermost boulder deposits.

Finally, the uppermost boulder-rich beds display no bedding or sorting. A fluvial origin is suggested from the presence of relatively well-rounded boulders, but compared to those observed at Miners Castle, it might correspond to higher energy and higher density floods due to the poor sorting and absence of bedding. Moreover, the truncation of the underlying sandstones is consistent with energetic floods with erosive behaviors. Compared with Miners Castle, we infer that poorly sorted boulder conglomerates may be laterally equivalent to the boulders that lie as a residual lag at the top of Miners Castle after weathering of the corresponding strata, but are not equivalent to the bedded section of Miners Castle boulder conglomerates (Figure 9).

A synthetic interpretative sketch summarizes the findings made in this study by avoiding locations with scree and compiling the different facies observed in a single section (Figure 10). The lowermost part of the section is poorly visible in the studied location (apart of the light-toned deposits LL in Figure 4), while it is described extensively in Stack et al. (this issue) from observations close to Hawksbill Gap and Cape Nukshak where it forms part of the Shenandoah formation. From its similarity in tone and localization within the fan front, we interpret the recessive light-toned deposits (LL in Figure 4) as the lateral equivalent of the Hogwallow Flats member lacustrine deposits (Stack et al., this issue). The central part of the hillslope corresponds to deltaic deposits, highlighted by the steeply dipping foreset beds, and usually develops over 20 m of vertical extension. These beds may be the lateral equivalent of the Rockytop outcrop described at the top of the Shenandoah formation (Stack et al., this issue), and of the dipping beds observed at Franklin Cliffs and Cape Nukshak (Gupta et al., 2022).

Present above the foresets are various types of fluvial deposits (sandstones and conglomerates) which are interpreted as topset bed deposits and thus likely deposited by the rivers which fed Jezero Lake. The transition between topsets and foresets is consistently in the range of ca.  $-2,490$  to  $-2,500$  m in the studied region of the delta front, and slightly above (ca.  $-2,480$  m) in the Franklin Cliffs and Cape Nukshak area (Gupta et al., 2022). Further up stratigraphically are present massive, poorly sorted boulder conglomerates that truncate the underlying bedforms. They represent an energetic last stage of fluvial floods whose relationship to the Jezero Lake is not yet determined.

## 6. Implications for Fluvial Activity and Lake Evolution at Jezero Crater

### 6.1. A Highly Variable Fluvial Input

The boulder conglomerates observed at the top of the fan scarp were previously interpreted as resulting from late-stage floods (Mangold et al., 2021). However, it was left open whether these deposits were coeval with the presence of a lake in Jezero or post-dated lacustrine deposition. Our new observations show that the boulder conglomerates at Miners Castle are bedded and sorted and comprise meter thick sequences characteristic of energetic, but common gravel-bar river flows with lateral accretion characteristic of bank attached bars in rivers (e.g., Ghinassi et al., 2014; Leeder, 1982; Stokes et al., 2012; Thomas et al., 1987; Willis, 1989). Similar cobble or



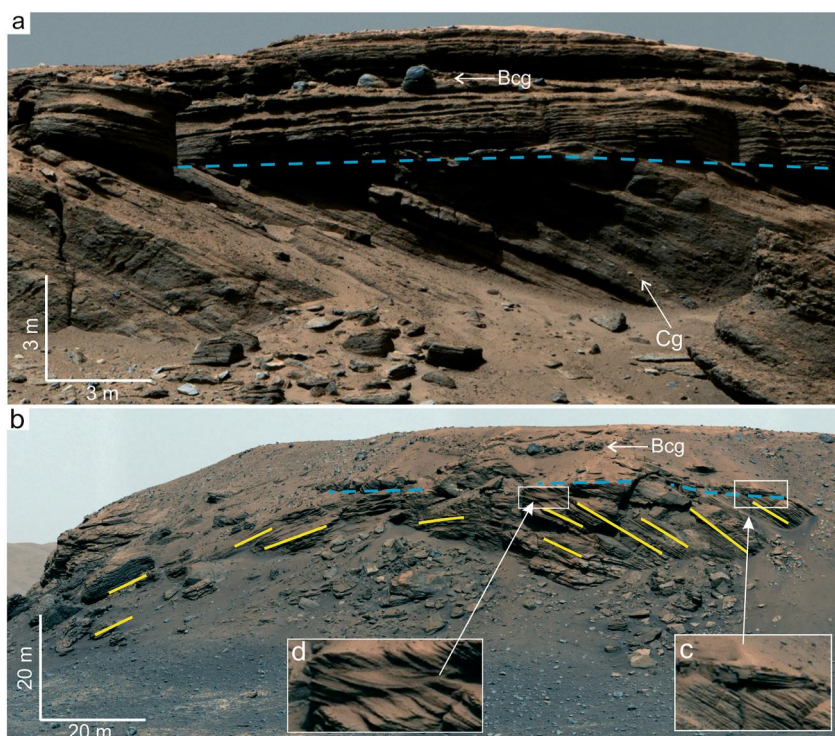


**Figure 11.** (a) Mastcam Z mosaic 110 mm of the Franklin Cliffs uppermost part, showing the transition from topset beds (subhorizontal, above the dashed blue line) to foreset beds (steeply dipping, under the blue line). (b) Mastcam Z mosaic of the antiformal structure of Whale Mountain (taken from Cape Nukshak in the southern edge of the fan, see Figure 1 for localization). The dashed blue line indicates the boundary between subhorizontal beds (topsets) overlying steeply dipping beds with opposite strike direction (highlighted locally by yellow drawing lines). The two insets show (c) the contact between the subhorizontal topsets and the steeply dipping foresets, and (d) the presence of a lens of backsets. This structure is interpreted as a mouth bar lobe, which has a lateral extent (~100 m) and thickness (~20 m) in the same range as the two antiformal structures observed at the Eastern Cape. Boulder conglomerate (Bcg) is present within topset beds in both examples (a) and (b). Pebble conglomerate (Cg) is present within the forests at Franklin Cliffs, showing that foresets can locally be fed by coarser material than sand.

boulder conglomerates have been observed in scarp C (Cg in Figure 7c) and in locations named Franklin Cliffs and Whale Mountain on the southern fan front (Bcg in Figures 11a and 11b), where they are part of the topset sequence (Gupta et al., 2022) and thus form part of the fluvial flows feeding the delta. At Moro rock, which is devoid of cobbles, fluvial sandstones (such as Ss in Figure 2c) may have been the main input of sediments rather than the coarse Miners Castle. Nevertheless, some of the foreset beds observed at Kodiak (Caravaca et al., this issue; Mangold et al., 2021) and at Franklin Cliffs (Cg in Figure 11a) display conglomeratic material that indicates a sediment source, which includes a coarse component of the fluvial input such as that observed at Miners Castle.

In contrast, both boulder conglomerates observed at the top of scarps C and D (Figures 7b, 7c, 11a, and 11b), as well as at the top of Kodiak (Caravaca et al., this issue; Mangold et al., 2021) sharply incise the underlying sandstone. In addition, they show no obvious evidence of sorting or bedding. These conglomerates seem to be related to more energetic episodes than what is recorded at Miners Castle. Their systematic presence at the uppermost section of scarps may indicate a direct link with the boulder-rich unit at the top of the delta, which has been interpreted as inverted channels (Goudge et al., 2018; Stack et al., 2020). Thus, our interpretation of this sequence of conglomerates is that they developed as two episodes or as a progressive transition from fluvial deposits initially coeval to the Jezero Lake (i.e., Miners Castle) toward more energetic boulder deposits corresponding to those mapped atop the delta (Stack et al., 2020). These more energetic boulder deposits may be potentially disconnected from the lake activity as their sharp eroded base could imply an unconformity, although we have no way to constrain the chronology from our observations.

Our results also highlight a strong variability in facies, and then in the strength of flows feeding the lake in Jezero, as suggested by the presence of both sandstone (Ss in Figures 2 and 7c subhorizontal sandstones) and boulder

conglomerates (Miners Castle, Figures 2 and 5c) at the same elevation. The origin of this variability as well as that of the high discharge represented by the boulder conglomerate is still unknown. Realistic hypotheses include seasonal variations due to melting of snow, glacial input with possible episodic surges punctuating more regular fluvial input, or arid climate type of flows with intense storms and related flash floods. We do not speculate further about the nature of fluvial activity in this study. However, the variability and the presence of high discharge rates have important implications on the lake evolution. Firstly, previous modeling of Jezero delta formation used steady-state discharge rates to estimate the time required to form the delta (Salese et al., 2020), an assumption that we can no longer justify according to our observations. Secondly, estimates of discharge rates in Section 4 (from  $\sim 100$  to  $\sim 500 \text{ m}^3 \text{ s}^{-1}$ ) may be used as upper limits for some of the peak discharge rates, although the number of flood events is still difficult to determine from the sparse outcrops and the ubiquitous presence of scree. Lastly, the variability of the fluvial input suggested by these flood events, if coeval to the lake, may also explain some of the lake level fluctuations suggested by observations made at Kodiak (Mangold et al., 2021, Caravaca et al., this issue).

## 6.2. Deltaic Geometry and Lake Level Variability

Overall, our observations confirm the Gilbert delta architecture of the delta front, with the classical tripartite architecture (e.g., Dietrich et al., 2016; Gilbert, 1885; Gobo et al., 2015; Longhitano, 2008; Nemeč, 1990; Postma, 1990; Rohais et al., 2008), from fluvial topsets on top toward foresets and bottomsets, although the latter are poorly expressed in the studied area. An interpretation as fluvial bars such as those observed in meander belts is not favored, especially because the thickness of the foresets is  $\sim 20$ – $25$  m in all locations where they are observed on the fan front. Assuming gravity played a minor role in channel dimensions (Konsoer et al., 2018), such a thickness for fluvial bars would require a km-wide channel with a km-scale meander wavelength based on terrestrial empirical relations, dimensions one order of magnitude higher than observed (see Section 5). In addition, all steeply dipping beds interpreted as foresets occur in the middle section of the fan front stratigraphy and are systematically underlain by planar stratified recessively weathering strata. No channel-shaped sedimentary bodies or cross-bedded strata typical of deposition by fluvial flows are visible in this middle section of the fan front. However, channel deposits such as Miners Castle and cross-bedded strata are well-observed in the upper section of the fan front stratigraphy in units interpreted as topsets, which consistently overlie the steeply dipping beds. Finally, we can also point out that Whale Mountain dipping beds display locally strata developed in lenses, namely backsets similar to those observed in foresets due to supercritical flows and hydraulic jump on the steep delta slope (e.g., Dietrich et al., 2016; Longhitano, 2008; Nemeč, 1990).

Our study also enables a higher resolution understanding of the organization of the deltaic deposits based on the observations of antiformal geometry of the deltaic foresets. Indeed, foreset beds at the Eastern Cape are organized in two  $\sim 80$ – $100$  m wide antiformal structures (A1 and A2 in Figure 4). Other antiformal structures, similar in scale to those observed at Eastern Cape, are observed on the front of the delta at Cape Nukshak in the outcrop informally named Whale Mountain (Figure 11b) (Gupta et al., 2022), and at Kodiak (Caravaca et al., this issue). These examples show that antiformal structures at the Eastern Cape are not unique to the eastern part of the fan. From the interpretation we made of the facies and geometry, we deduce that these structures are the preserved remnants of individual deltaic lobes, referred to as mouth bars in the deltaic nomenclature, or mouth bar accretion element for the smallest lobe formed by this process (Figure 12) (e.g., Cole et al., 2021; Olairu & Bhattacharya, 2006). The presence of mouth bars of such dimensions may represent the smallest components of deltaic growth, with the amalgamation of several mouth bars defining the development of deltaic lobes, as is common on Earth (e.g., Cole et al., 2021; Olairu & Bhattacharya, 2006; Wellner et al., 2005). Each accretion element appears as a small lobe in planview, and as an antiformal shape in cross-section (Figure 12). The dimensions of the mouth bars and their accretion elements are directly related to the water depth within the Jezero Lake and the size of the incoming river (e.g., Cole et al., 2021). In the case of the Eastern Cape, the lake depth is estimated to be more than 45 m from the current crater floor elevation ( $-2,545$  m). Nevertheless, the recessive light-toned deposits below Moro Rock (LL in Figure 4) may already have been present at the time of the foreset deposition (e.g., deltaic progradation over former lake deposits, i.e., bottomset beds). In that case, the lake depth would have been  $\sim 25$  m, which is still substantial. From a purely geometric view, the size of these elemental accretion lobes is consistent with a formation within 30–45 m wide river channels, thus consistent with the channel dimension estimated at Miners Castle. Indeed, the lobe shape implies that the incoming river is narrower than the width of the mouth bars, here 80–100 m (Figure 12).

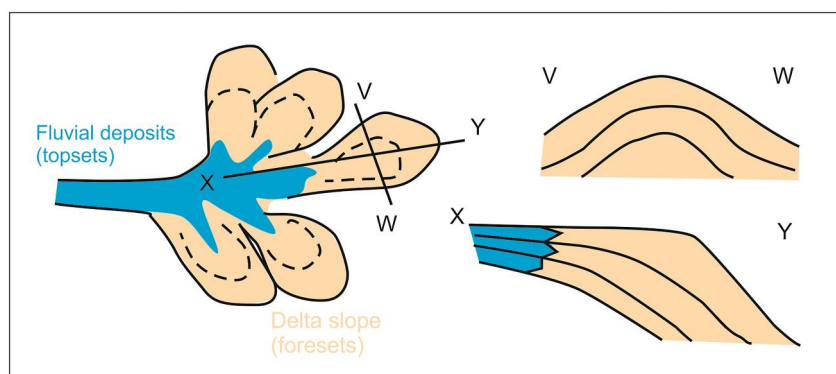


**Figure 12.** Plan view of a delta mouth bar composed of five accretion elements representing the smallest lobe structure on a delta (adapted from Cole et al., 2021). This architecture implies that the inlet river width is smaller than that of each accretion element.

Our observations at the Eastern Cape also enable tracing foreset beds further north where Goudge et al. (2017) identified a series of potential topset and foreset beds from orbital data. Foresets observed in our study are locally up to  $32^\circ$  steep and generally above  $10^\circ$  where apparent dips can be measured. These dips are higher than the dips measured by Goudge et al. (2017), who interpreted foreset geometries with dips of  $2\text{--}10^\circ$ . Unfortunately, the outcrops studied by Goudge et al. (2017) are located north of the Eastern Cape and were not visible by the rover along its traverse, precluding in situ observations. The strata interpreted as foresets in Goudge et al. (2017) are located between elevations of ca.  $-2,500$  m and ca.  $-2,470$  m. Some of them are located mid-slope and comparable in aspect to some observed here. Their slightly higher elevation could represent higher lake phases (Mangold et al., 2023). In this case, the lower dip might be due to an underestimation of the real dip from orbital data.

Lastly, our interpretation of Moro Rock and scarp C leads to a lake level that would be located at an elevation of ca.  $-2,490\text{--}2,500$  m at the time of deposition. This is the same elevation range as observed at Kodiak (Mangold et al., 2021, Caravaca et al., this issue). Thus, it provides a useful point of comparison from an outcrop that is part of the fan 4 km north of the Kodiak remnant butte, suggesting that these delta lobes prograded to the east almost coevally to those observed at Kodiak, which prograded to the south. These inferred lake levels are also located 10 m below the elevation reported at Franklin Cliffs on the southern delta front (Figure 11a) (Gupta et al., 2022). These deltaic deposits are overall consistent with the view that the delta is dominantly progradational in its structure and was deposited during an overall fall of the lake level, in agreement with the elevations reported for higher topset-foreset transition on the delta top, up to elevations of ca.  $-2,410$  m (Mangold et al., 2023).

## 7. Conclusions

The easternmost strata cropping out along the front of Jezero western fan has been imaged at a spatial resolution three times better than initial observations acquired from the landing area. The lower interval of the fan front is poorly visible due to scree and only patchy, light toned deposits are observed. We interpret these strata as laterally equivalent to the Hogwallow Flat member observed along the rover traverse (Stack et al., this issue). The middle of the hillslopes comprised planar bedded sandstones with gentle to high dips (up to  $32^\circ$ ) distributed in distinct sedimentary bodies. At the Eastern Cape, these beds represent two antiformal shapes at scales of  $80\text{--}100$  m in width and  $20\text{--}25$  m in height. These structures are interpreted as delta mouth bars or individual accretion elements of mouth bars (e.g., Cole et al., 2021; Olairu & Bhattacharya, 2006), depositional elements typical of sediments entering into a standing body of water. The top of the delta mouth bars represented by the topset-foreset transition would represent the lake level at the time of deposition. This transition is observed at elevations of ca.  $-2,490$  m to  $-2,500$  m in two locations. These elevations are consistent with the lake level elevations deduced at Kodiak from the same bed type (Caravaca et al., this issue; Mangold et al., 2021), and are slightly lower than those observed at the southern fan front (Gupta et al., 2022), suggesting that these strata are time equivalent. These new observations led us to confirm a deltaic origin for this portion of the Jezero western fan, consistent with the initial depositional interpretations of the Kodiak butte (Mangold et al., 2021). The presence of deltaic foresets in the fan front is also in agreement with the conclusions made from orbital data by Goudge et al. (2017, 2018), but the overall organization suggests formation during lake level fall rather than during lake level rise.



Our new observations also lead to several new conclusions regarding fluvial deposition within this section. The cobble-boulder conglomerate beds at Miners Castle are confirmed as fluvial flood deposits, with additional observations pointing toward the presence of a clear bedding with meter-scale fining-upward sequences. Nevertheless, this conglomerate is observed only a few meters above the beds interpreted as delta mouth bars, suggesting that these fluvial flows, for which we estimate discharge rates of  $\sim 100\text{--}500\text{ m}^3\text{ s}^{-1}$ , were involved in feeding Jezero Lake. These conglomerate beds/bodies are also surrounded by finer-grained sandstones from less energetic fluvial episodes. This variability in fluvial deposition should be taken into account in numerical models of deltaic deposition.

The boulder conglomerates observed in the uppermost section of several scarps along the fan front truncate the underlying sandstone, and are apparently massive, without obvious bedding or clast sorting, a sequence suggestive of higher-energy fluvial floods compared to the Miners Castle deposit. These differences suggest that distinct flood types or a transition from one to the other archive an increase in extreme events that conclude with the uppermost boulder deposits. The presence of a boulder-rich lag at the top of these hillslopes shows that these deposits are likely linked to the Delta blocky unit observed from orbital data (Stack et al., 2020). Glacial surges, heavy seasonal snowmelts, or arid climate flash floods from storms could equally explain the trigger for these floods. Although the nature of these episodic flood events remains unexplained, and their genetic link to the fluvial beds that they truncate is uncertain, these uppermost boulder deposits likely represent the last gasp of liquid water at the surface in Jezero crater.

### Data Availability Statement

All images used in this study are available on the Planetary Data System (PDS): <https://pds-geosciences.wustl.edu/m2020/>. Detailed image numbers and links to data of the Perseverance rover SuperCam and Mastcam-Z instruments used are [https://pds-geosciences.wustl.edu/m2020/urn-nasa-pds-mars2020\\_supercam/data\\_radcal\\_rmi/](https://pds-geosciences.wustl.edu/m2020/urn-nasa-pds-mars2020_supercam/data_radcal_rmi/) and [https://pds-imaging.jpl.nasa.gov/data/mars2020/mars2020\\_mastcamz/data\\_asu/rad](https://pds-imaging.jpl.nasa.gov/data/mars2020/mars2020_mastcamz/data_asu/rad), and are listed in Tables S1 and S2 in Supporting Information S1 (Bell & Maki, 2021; Maurice & Wiens, 2021). Mars reconnaissance Orbiter High Resolution Imaging Science Experiment (HiRISE) data (McEwen, 2007) used for Figures 1 and 4 and elevation scales in Figures 2 and 7 are available using the following links: [https://hirise-pds.lpl.arizona.edu/PDS/EDR/ESP/ORB\\_036600\\_036699/ESP\\_036618\\_1985/](https://hirise-pds.lpl.arizona.edu/PDS/EDR/ESP/ORB_036600_036699/ESP_036618_1985/), [https://hirise-pds.lpl.arizona.edu/PDS/EDR/ESP/ORB\\_037100\\_037199/ESP\\_037119\\_1985/](https://hirise-pds.lpl.arizona.edu/PDS/EDR/ESP/ORB_037100_037199/ESP_037119_1985/), [https://hirise-pds.lpl.arizona.edu/PDS/EDR/PSP/ORB\\_002300\\_002399/PSP\\_002387\\_1985/](https://hirise-pds.lpl.arizona.edu/PDS/EDR/PSP/ORB_002300_002399/PSP_002387_1985/), [https://hirise-pds.lpl.arizona.edu/PDS/EDR/PSP/ORB\\_003700\\_003799/PSP\\_003798\\_1985/](https://hirise-pds.lpl.arizona.edu/PDS/EDR/PSP/ORB_003700_003799/PSP_003798_1985/) and the DEM (Ferguson et al., 2020).

### References

- Alexander, J., & Cooker, M. J. (2016). Moving boulders in flash floods and estimating flow conditions using boulder in ancient deposits. *Sedimentology*, 63(6), 1582–1595. <https://doi.org/10.1111/sed.12274>
- Attal, M., & Lavé, J. (2006). Changes of bedload characteristics along the Marsyandi River (Central Nepal). *Geological Society of America, Special Publication*. Paper 398.
- Bathurst, J. C. (1985). Flow resistance estimation in mountain rivers. *Journal of Hydrologic Engineering*, 11(4), 625–643. [https://doi.org/10.1061/\(asce\)0733-9429\(1985\)11:4\(625\)](https://doi.org/10.1061/(asce)0733-9429(1985)11:4(625))
- Bell, J. F., III, Maki, J. N., Mehall, G. L., Ravine, M. A., Caplinger, M. A., Bailey, Z. J., et al. (2020). The Mars 2020 rover mast camera zoom (Mastcam-Z) multispectral, stereoscopic imaging investigation. *Space Science Reviews*, 217(1), 24. <https://doi.org/10.1007/s11214-020-00755-x>
- Bell, J. F., & Maki, J. M. (2021). Mars 2020 mast camera zoom bundle [Dataset]. *NASA Planetary Data System*. <https://doi.org/10.17189/1522843>
- Caravaca, G., Dromart, G., Mangold, N., Gupta, S., Tate, C., Randazzo, N., et al. Depositional facies and sequence stratigraphy of the Kodiak butte, western Delta of Jezero crater, Mars. (this issue).
- Cole, G., Jerrett, R., & Watkinson, M. P. (2021). A stratigraphic example of the architecture and evolution of shallow water mouth bars. *Sedimentology*, 68(3), 1227–1254. <https://doi.org/10.1111/sed.12825>
- Costa, J. E. (1983). Paleohydraulic reconstruction of flash-flood peaks from boulder deposits in the Colorado Front Range. *Geological Society of America Bulletin*, 94(8), 986–1004. [https://doi.org/10.1130/0016-7606\(1983\)94<986:profpf>2.0.co;2](https://doi.org/10.1130/0016-7606(1983)94<986:profpf>2.0.co;2)
- Dietrich, P., Ghienne, J.-F., Normandeau, A., & Lajeunesse, P. (2016). Upslope migrating bedforms in a proglacial sandur delta: Cyclic steps from river-derived underflows? *Journal of Sedimentary Research*, 86(2), 113–123. <https://doi.org/10.2110/jsr.2016.4>
- Ehlmann, B. L., Mustard, J. F., Fassett, C. I., Schon, S. C., Head, J. W., III, Des Marais, D. J., et al. (2008). Clay minerals in delta deposits and organic preservation potential on Mars. *Nature Geoscience*, 1(6), 355–358. <https://doi.org/10.1038/ngeo207>
- Fassett, C. I., & Head, J. W. (2005). Fluvial sedimentary deposits on Mars: Ancient deltas in a crater lake in the Nili Fossae region. *Geophysical Research Letters*, 32(14), L14201. <https://doi.org/10.1029/2005GL023456>
- Ferguson, R. L., Galuszka, D. M., Hare, T. M., Mayer, D. P., & Redding, B. L. (2020). Mars 2020 Terrain relative navigation HiRISE orthorectified image mosaic [dataset]. *U.S. Geological Survey*. <https://doi.org/10.5066/P9QJDP48>
- Ghinassi, M., Nemeč, W., Aldinucci, M., Nehyba, S., Özaksoy, V., & Fidolini, F. (2014). Plan-form evolution of ancient meandering rivers reconstructed from longitudinal outcrops sections. *Sedimentology*, 61(4), 952–977. <https://doi.org/10.1111/sed.12081>

### Acknowledgments

The authors thank the thorough comments made by Sharon Wilson and William McMahon. The authors acknowledge the Mars 2020 team members who participated in tactical and strategic science operations as well as the Mars 2020 project management and engineers for their continuous efforts in making this mission a success. French authors are granted by the Centre National d'Etudes Spatiales (CNES). Joanneum Research received funding from the Austrian Research Promotion Agency, ASAP-18 Project 892662 "Mars-3D." RCW is granted by NASA contract NNH13ZDA0180. RMEW is granted by JPL Subcontract 1685864. LCK is granted by the M2020 SHERLOC-WATSON Instrument Team. KMS's effort was carried out at the Jet Propulsion Laboratory, California Institute of Technology under a contract with the National Aeronautics and Space Administration.

- Gilbert, G. K. (1885). *The topographic features of lake shores*. 5th Annual Report (pp. 69–123). United States Geol. Survey.
- Gobo, K., Ghinassi, M., & Nemeč, W. (2015). Gilbert-type deltas recording short-term base-level changes: Delta-brink morphodynamics and related foreset facies. *Sedimentology*, 62(7), 1923–1949. <https://doi.org/10.1111/sed.12212>
- Goudge, T. A., Head, J. W., Mustard, J. F., & Fassett, C. I. (2012). An analysis of open-basin lake deposits on Mars: Evidence for the nature of associated lacustrine deposits and post-lacustrine modification processes. *Icarus*, 219(1), 211–229. <https://doi.org/10.1016/j.icarus.2012.02.027>
- Goudge, T. A., Milliken, R. A., Head, J. W., Mustard, J. F., & Fassett, C. I. (2017). Sedimentological evidence for a deltaic origin of the western fan deposit in Jezero crater, Mars and implications for future exploration. *Earth and Planetary Science Letters*, 458, 357–365. <https://doi.org/10.1016/j.epsl.2016.10.056>
- Goudge, T. A., Mohrig, D., Cardenas, B. T., Hughes, C. M., & Fassett, C. I. (2018). Stratigraphy and paleohydrology of delta channel deposits, Jezero crater, Mars. *Icarus*, 301, 58–75. <https://doi.org/10.1016/j.icarus.2017.09.034>
- Goudge, T. A., Mustard, J. F., Head, J. W., Fassett, C. I., & Wiseman, S. M. (2015). Assessing the mineralogy of the watershed and fan deposits of the Jezero crater paleo-lake system, Mars. *Journal of Geophysical Research*, 120(4), 775–808. <https://doi.org/10.1002/2014JE004782>
- Gupta, S., Mangold, N., Caravaca, G., Gasnault, O., Dromart, G., Tarnas, J. D., et al. (2022). A delta-lake system at Jezero crater (Mars) from long distance observations. *Lunar and Planetary Science Conference 53th*. abstract 2295.
- Hayes, A. G., Corlies, P., Tate, C., Barrington, M., Bell, J. F., Maki, J. N., et al. (2021). Pre-flight calibration of the Mars 2020 rover Mastcam Zoom (Mastcam-Z) multispectral, stereoscopic imager. *Space Science Reviews*, 217(2), 29. <https://doi.org/10.1007/s11214-021-00795-x>
- Kinch, K. M., Madsen, M. B., Bell, J. F., Maki, J. N., Bailey, Z. J., Hayes, A. G., et al. (2020). Radiometric calibration targets for the Mastcam-Z camera on the Mars 2020 rover mission. *Space Science Reviews*, 216(8), 141. <https://doi.org/10.1007/s11214-020-00774-8>
- Kleinmans, M. E. (2005). Flow discharge and sediment transport model for estimating a minimum timescale of hydrological activity of channel and delta formation on Mars. *Journal of Geophysical Research*, 110(E12), E12003. <https://doi.org/10.1029/2005je002521>
- Konsoer, K. M., LeRoy, J., Burr, D., Parker, G., Jacobsen, R., & Turnel, D. (2018). Channel slope adjustment in reduced gravity environments and implications for Martian channels. *Geology*, 2018044.
- Leeder, M. R. (1982). *Sedimentology: Process and product* (p. 344pp). Chapman and Hamm.
- Longhitano, S. (2008). Sedimentary facies and sequence stratigraphy of coarse-grained Gilbert-type deltas within the Pliocene thrust-top Potenza Basin (Southern Apennines, Italy). *Sedimentary Geology*, 210(3–4), 87–110. <https://doi.org/10.1016/j.sedgeo.2008.07.004>
- Malin, M. C., Bell, J. F., Cantor, B. A., Caplinger, M. A., Calvin, W. M., Clancy, R. T., et al. (2007). Context camera investigation on board the Mars reconnaissance orbiter. *Journal of Geophysical Research*, 112(E5), E05S04. <https://doi.org/10.1029/2006JE002808>
- Mangold, N., Caravaca, G., Gupta, S., Williams, R., Dromart, G., Gasnault, O., et al. (2023). *The formation of the fluvio-deltaic deposits of western fan of Jezero crater, Mars, during lake-level fall*. Am. Geophys. Union Fall Conference.
- Mangold, N., Dromart, G., Ansan, V., Massé, M., Salese, F., Kleinmans, M., et al. (2020). Fluvial regimes, age and duration of Jezero crater paleolake and its significance for the 2020 rover mission landing site. *Astrobiology*, 20(8), 994–1013. <https://doi.org/10.1089/ast.2019.2132>
- Mangold, N., Gupta, S., Gasnault, O., Dromart, G., Tarnas, J. D., Sholes, S. F., et al. (2021). Perseverance rover reveals an ancient delta-lake system and flood deposits at Jezero crater, Mars. *Science*, 374(6568), 711–717. <https://doi.org/10.1126/science.abl4051>
- Maurice, S., Wiens, R. C., Bernardi, P., Caïs, P., Robinson, S., Nelson, T., et al. (2021). The SuperCam instrument suite on the NASA Mars 2020 rover: Mast Unit and calibration targets. *Space Science Reviews*, 217(3), 47. <https://doi.org/10.1007/s11214-021-00807-w>
- Maurice, S. A., & Wiens, R. C. (2021). Mars 2020 SuperCam bundle [Dataset]. *NASA Planetary Data System*. <https://doi.org/10.17189/1522646>
- McEwen, A. S. (2007). MRO Mars high resolution imaging science experiment RDR V1.1 [Dataset]. *NASA Planetary Data System*. <https://doi.org/10.17189/1520303>
- McEwen, A. S., Eliason, E. M., Bergstrom, J. W., Bridges, N. T., Hansen, C. J., Delamere, W. A., et al. (2007). Mars reconnaissance orbiter's high resolution imaging science experiment (HiRISE). *Journal of Geophysical Research*, 112(E5), E05S02. <https://doi.org/10.1029/2005JE002605>
- Nemeč, W. (1990). Aspects of sediment movement on steep delta slopes. In A. Colella & D. B. Prior (Eds.), *Coarse-grained deltas* (Vol. 10, pp. 29–73). International Association of Sedimentologists Special Publication.
- Olairu, C., & Bhattacharya, J. P. (2006). Terminal distributary channels and delta front architecture of river-dominated delta systems. *Journal of Sedimentary Research*, 76(2), 212–233. <https://doi.org/10.2110/jsr.2006.026>
- Paar, G., Ortner, T., Tate, C., Deen, R. G., Abercrombie, P., Vona, M., et al. (2023). Three-dimensional data preparation and immersive mission-spanning visualization and analysis of Mars 2020 Mastcam-Z stereo image sequences. *Earth and Space Science*, 10(3). <https://doi.org/10.1029/2022EA002532>
- Postma, G. (1990). Depositional architecture and facies of river and fan deltas: A synthesis. In A. Colella & D. B. Prior (Eds.), *Coarse-grained deltas* (Vol. 10, pp. 13–27). International Association of Sedimentologists Special Publication.
- Rohais, S., Eschard, R., & Guillocheau, F. (2008). Depositional model and stratigraphic architecture of rift climax Gilbert-type fan deltas (Gulf of Corinth, Greece). *Sedimentary Geology*, 210(3–4), 132–145. <https://doi.org/10.1016/j.sedgeo.2008.08.001>
- Salese, F., Kleinmans, M., Mangold, N., De Haas, T., Ansan, V., McMahon, W., et al. (2020). Estimated minimum lifetime of the Jezero crater Delta, Mars. *Astrobiology*, 20(8), 977–993. <https://doi.org/10.1089/ast.2020.2228>
- Schon, S. C., Head, J. W., & Fassett, C. I. (2012). An overfilled lacustrine system and progradational delta in Jezero crater, Mars: Implications for Noachian climate. *Planetary and Space Science*, 67(1), 28–45. <https://doi.org/10.1016/j.pss.2012.02.003>
- Smith, D. E., Zuber, M. T., Solomon, S. C., Phillips, R. J., Head, J. W., Garvin, J. B., et al. (1999). The global topography of Mars and implications for surface evolution. *Science*, 284(5419), 1495–1503. <https://doi.org/10.1126/science.284.5419.1495>
- Stack, K. M., Ives, L. R. W., Gupta, S., Lamb, M. P., Telbot, M., Caravaca, G., et al. Sedimentology and stratigraphy of the Shenandoah formation. Western Sediment Fan, Jezero Crater, Mars. (this issue).
- Stack, K. M., Williams, N. R., Calef III, F., Sun, V. Z., Williford, K. H., Farley, K. A., et al. (2020). Photogeologic map of the perseverance rover field site in Jezero crater constructed by the Mars 2020 science team. *Space Science Review*, 216, 127. <https://doi.org/10.1007/s11214-020-00739>
- Stokes, M., Griffiths, J. S., & Mather, A. (2012). Paleoflood estimates of Pleistocene coarse grained river terrace landforms (Rio Almanzora, SE Spain). *Geomorphology*, 149–150, 11–26. <https://doi.org/10.1016/j.geomorph.2012.01.007>
- Thomas, R. G., Smith, D. G., Wood, J. M., Visser, J., Calverley-Range, E. A., & Koster, E. H. (1987). Inclined heterolithic stratification terminology, description, interpretation and significance. *Sedimentary Geology*, 53(1–2), 123–179. [https://doi.org/10.1016/0037-0738\(87\)90059-5](https://doi.org/10.1016/0037-0738(87)90059-5)
- Wellner, R., Beaubouef, R., Van Wagoner, J., Roberts, H. H., & Sun, T. (2005). Jet-plume depositional bodies: the primary building blocks of Wax Lake Delta. *Transactions - Gulf Coast Association of Geological Societies*, 55, 857–909.

- Wiens, R., Maurice, S., Robinson, S. H., Nelson, A. E., Cais, P., Bernardi, P., et al. (2021). The SuperCam instrument suite on the NASA Mars 2020 rover: Body unit. *Space Science Reviews*, 217, 4.
- Williams, G. P. (1986). River meanders and channel size. *Journal of Hydrology (Wellington North)*, 88(1–2), 147–164. [https://doi.org/10.1016/0022-1694\(86\)90202-7](https://doi.org/10.1016/0022-1694(86)90202-7)
- Willis, B. J. (1989). Paleochannel reconstructions from point bar deposits: A 3D perspective. *Sedimentology*, 36(5), 757–766. <https://doi.org/10.1111/j.1365-3091.1989.tb01744.x>
- Wilson, L., Ghatan, G. J., Head, J. W., III, & Mitchell, K. L. (2004). Mars Outflow channels: A reappraisal of the estimation of water flow velocities from water depths, regional slopes and channel floor properties. *Journal of Geophysical Research*, 109(E9), E09003. <https://doi.org/10.1029/2004je002281>